Diamond & Related Materials 128 (2022) 109225

Contents lists available at ScienceDirect

Diamond & Related Materials

journal homepage: www.elsevier.com/locate/diamond

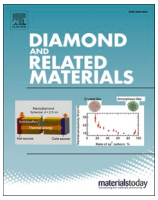

The effect of boron concentration on the electrical, morphological and optical properties of boron-doped nanocrystalline diamond sheets: Tuning the diamond-on-graphene vertical junction

Michał Rycewicz [a,b], Adrian Nosek [c], Dong Hoon Shin [b,d], Mateusz Ficek [a], Josephus G. Buijnsters [b,*], Robert Bogdanowicz [a]

[a] Department of Metrology and Optoelectronics, Gdańsk University of Technology, Narutowicza 11/12, 80-233 Gdańsk, Poland
[b] Department of Precision and Microsystems Engineering, Delft University of Technology, Mekelweg 2, 2628 CD Delft, the Netherlands
[c] Department of Physics, University of California Riverside, University Avenue 900, 92521 Riverside, USA
[d] Kavli Institute of Nanoscience, Delft University of Technology, Lorentzweg 1, 2628 CJ Delft, the Netherlands

ARTICLE INFO

Keywords:
Boron-doped diamond (BDD)
Nanocrystalline sheets
Electrical conductivity
Heterojunction
Graphene

ABSTRACT

In this paper, the effect of boron doping on the electrical, morphological and structural properties of free-standing nanocrystalline diamond sheets (thickness ~ 1 μm) was investigated. For this purpose, we used diamond films delaminated from a mirror-polished tantalum substrate following a microwave plasma-assisted chemical vapor deposition process, each grown with a different [B]/[C] ratio (up to 20,000 ppm) in the gas phase. The developed boron-doped diamond (BDD) films are a promising semiconducting material for sensing and high-power electronic devices due to band gap engineering and thermal management feasibility. The increased boron concentration in the gas phase induces a decrease in the average grain size, consequently resulting in lower surface roughness. The BDD sheets grown with [B]/[C] of 20,000 ppm reveal the metallic conductivity while the lower doped samples show p-type semiconductor character. The charge transport at room temperature is dominated by the thermally activated nearest-neighbor hopping between boron acceptors through impurity band conduction. At low temperatures (<300 *K*), the Arrhenius plot shows a non-linear temperature dependence of the logarithmic conductance pointing towards a crossover towards variable range hopping. The activation energy at high temperatures obtained for lowly-doped sheets is smaller than for nanocrystalline diamond bonded to silicon, while for highly-doped material it is similar. Developed sheets were utilized to fabricate two types of diamond-on-graphene heterojunctions, where boron doping is the key factor for tuning the shape of the current-voltage characteristics. The graphene heterojunction with the low boron concentration diamond sheet resembles a Schottky junction behavior, while an almost Ohmic contact response is recorded with the highly doped BDD sheet of metallic conductivity. The free-standing diamond sheets allow for integration with temperature-sensitive interfaces (i.e. 2D materials or polymers) and pave the way towards flexible electronics devices.

1. Introduction

Diamond has excellent properties for future electronics, such as its high carrier mobility [1,2], high breakdown field [3,4], high thermal conductivity [5], emission stability [6], low dielectric constant and possibility of doping [7,8]. Doped with sulfur or phosphorus, diamond behaves like an n-type semiconductor [9]. A single electron at a nitrogen-vacancy can be controlled by radio waves and it behaves like a qubit, useful for quantum memories [10]. In the case of boron doping, a p-type semiconductor can be obtained. Due to its small atomic size, boron easily incorporates into the diamond lattice [11]. At low temperatures, boron-doped diamond (BDD) exhibits superconductivity with the superconducting transition temperature $T_c = 4$ K, which varies with doping level [12–14].

The above properties make diamond an attractive material for high-frequency and high-power devices. Recently, Jha et al. [15] fabricated Schottky p-i-n diodes for high-power RF receiver protectors based on single-crystal diamond, which are able to protect up to 100 W (50 dBm)

* Corresponding author.
E-mail address: J.G.Buijnsters@tudelft.nl (J.G. Buijnsters).

https://doi.org/10.1016/j.diamond.2022.109225
Received 11 May 2022; Received in revised form 15 June 2022; Accepted 5 July 2022
Available online 9 July 2022

of input power. At high temperatures, diamond Schottky barrier diodes show low leakage current and high breakdown field (1.8 kV at 300 K) [16]. In case of polycrystalline films, nanocrystalline superconducting diamond resonators demonstrate the potential for sensitive inductance detectors [17]. Recently, Klemencic et al. [18] showed that the columnar crystal structure of boron-doped nanocrystalline diamond forms an intrinsic Josephson junction array. Change of the superconducting states is possible by applying electromagnetic noise pulses. Moreover, nanocrystalline diamond can be used as a field effect transistor to detect proteins or DNA [19,20]. However, with high carrier density, it is difficult to achieve high mobility [21]. The possible solution is to use hexagonal boron nitride as a gate dielectric [22].

The combination of diamond with other, two-dimensional, materials is also achievable. To provide higher electrochemical capacitance, nanodiamonds were chemically conjugated with molybdenum disulfide [23]. MoS_2 on diamond with a graphitic shell was reported to reduce the diffusion distance of ions and electrons leading to excellent electrochemical performance of the nanocomposite electrode. Zhao et al. [24] reported that diamond as supporting material for graphene can overcome the thermal capacity issue and improve carrier transport characteristics of graphene devices. On the other hand, nanodiamond-on-graphene decreases the sheet conductivity showing significant negative magnetoresistance at low temperatures [25]. Recently, we have presented [26] a new method for realizing diamond membranes and transporting them onto graphene substrates to obtain low-temperature devices, such as field-effect transistor-like devices. Thin diamond membranes can be used as pressure sensors for harsh environments [27], electrochemical sensors [28] or electronic devices [29]. Additionally, diamond thin single-crystal films exhibit high uniform tensile elasticity [30] allowing for their use in flexible and high-power electronics.

Unfortunately, there is a significant lack of knowledge regarding the effects of boron on the optical, electrical and morphological properties of free-standing diamond films. Most studies focus on the effect of boron incorporation on single-crystal diamond [31], nanodiamond powder [32], or polycrystalline diamond films on silicon/quartz [33,34]. Janssens et al. [35] presented the influence of the [C]/[H] ratio on the transport properties of nanocrystalline boron-doped diamond with constant [B]/[C] ratio in the gas phase. By changing the boron concentration, the type of conductivity, optical band gap, and morphology of diamond were strongly modified [33,36–38]. Our previous research [26] manifested that medium boron-doped diamond sheets with [B]/[C] = 10,000 ppm in the gas phase form a junction with graphene but no doping impact nor morphological influence on the junction interface was revealed. The interactions between graphene and highly/lowly boron-doped diamond sheets are marginally reported up-to-date.

In this paper, for the first time, we report the electrical, morphological and optical properties of nanocrystalline diamond thin sheets as a function of boron doping. For this purpose, we used thin-film diamond sheets fully delaminated from tantalum. Additionally, as proof of principle, we studied the I-V characteristics of graphene coupled with low and highly doped diamond sheets, respectively.

2. Materials and methods

2.1. Preparation of diamond sheets

Free-standing BDD sheets with a thickness of 1.3 ± 0.3 μm were obtained by spontaneous delamination following growth on tantalum substrate (10 mm × 10 mm × 0.25 mm) in a microwave plasma-enhanced chemical vapor deposition reactor using CH_4 and H_2 plasma (1:100 M ratio). The deposition was performed using a Seki Technotron AX5400S system with the following parameters for 3 h: microwave power 1100 W; temperature 500 °C; pressure 50 Torr. Before growth, the mirror-polished tantalum substrates were seeded ultrasonically in an aqueous suspension containing nanodiamond powder (4–7 nm in size). The boron doping was controlled by adding diborane to the gas phase. We fabricated differently doped BDD sheet samples by varying the [B]/[C] ratio in the gas phase: undoped (0 ppm), lowly-doped (250, 500, 1000 ppm), medium-doped (5000, 10,000 ppm) and highly-doped (20,000 ppm). The various samples will be denoted by this [B]/[C] ratio from here onwards.

2.2. Structural and electrical characterization

The surface morphology was investigated using scanning electron microscopy (JSM-6500F, JEOL) in secondary electron imaging mode. To obtain the average size of the surface grains, we manually outlined every single grain in the specific surface area. Next, using Gwyddion software and following the planimetric procedure [39], we calculated the average projected area and mean planar grain radius (i.e., half of the mean planar grain diameter). A micro-Raman microscopy system (LabRAM HR, Horiba Scientific) operating at 514 nm wavelength was used to study the bonding structure of the BDD sheets. The laser output power was set to approx. 450 μW and a laser spot size of about 2 μm was used to probe the samples. The boron concentration was determined by Hall-effect measurements at room temperature using a Secondary Ion Mass Spectrometer (Atomika 4500, Cameca) and 0.55 T Hall-effect setup (HMS-3000, Ecopia). Before the measurements, the BDD sheets were transferred to (polydimethylsiloxane) PDMS, as reported previously in [40]. Next, the sheets were analyzed using Van der Pauw geometry with and without a magnetic field. For SIMS investigations, the diamond sheets were transported directly onto a p-type silicon substrate. The temperature dependence of the electrical conductivity was measured using the HFS600E-PB4 Linkam system, employing a sandwich configuration. The ohmic contacts for the top and bottom layers were made of Ti/Au. Charge transfer was observed through the diamond sheet structures. Optical absorbance measurements were done in the range from 340 nm to 1100 nm using a UV-9000 Metash system with a scan step of 1 nm. The optical band gap energy was obtained using Tauc's plot [41].

2.3. Fabrication of diamond-graphene vertical junction (D-on-G)

The fabrication procedure of the diamond-graphene junctions is presented in Fig. 1. Graphene (6 mm × 6 mm) on 300 nm SiO_2/Si (Graphenea, Spain) was patterned by lithography and etched by oxygen plasma to achieve 2.5 mm × 0.8 mm lines on SiO_2 (Etchlab 200, Sentach Instruments). Next, titanium (5 nm) and palladium (95 nm) layers were evaporated on the graphene edges and silicon dioxide for drain and source contacts (FC-2000, Temescal). At the end, diamond sheets ([B]/[C] = 500 ppm and 20,000 ppm, respectively) on PDMS were transferred on a graphene monolayer to form the D-on-G junctions. The nucleation surface had direct contact with the surface of graphene. Current-voltage characteristics of realized devices were obtained by a probe station (PM5, SÜSS MicroTec) and source measure unit (B2912A, Keysight).

3. Results and discussion

Scanning electron microscopy was used to evaluate the morphology of the growth and nucleation surfaces of the diamond sheets, shown in Fig. 2. Increased boron concentration in the gas phase results in smaller average grain size (Fig. 2 (a,b)) and consequently lower surface roughness. A particularly dramatic decline is observed in the range between 500 and 5000 ppm. Cifre et al. [42] suggested that boron enhances nucleus formation during the initial stage of diamond film growth. In addition, diamond renucleation processes occur during chemical vapor deposition [43,44] which are enhanced by applying a higher [B]/[C] ratio in the gas phase. As a consequence, the fabricated microstructures should exhibit different thermal and electrical conduction levels [36,45].

The samples do not exhibit any preferred crystalline orientation as a result of random nucleation. As was reported elsewhere [46], the

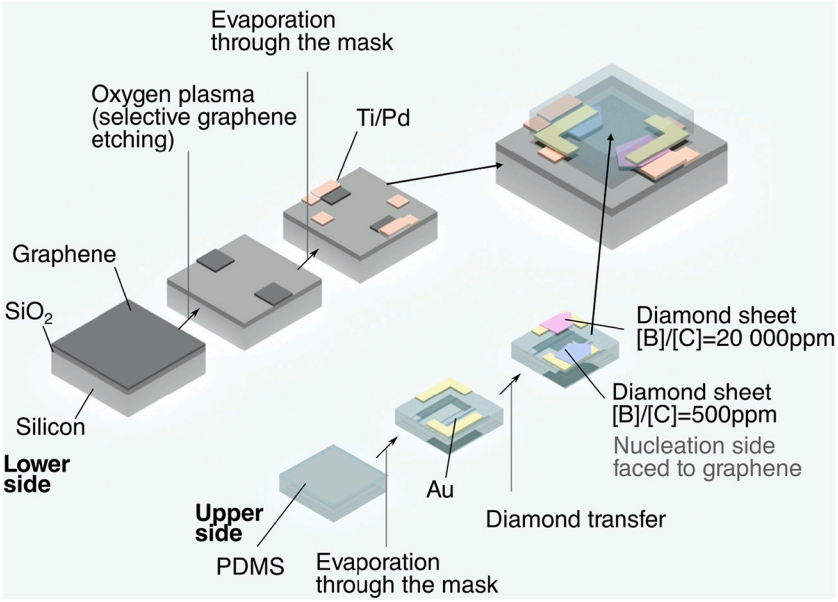

Fig. 1. The fabrication procedure of the diamond-graphene junctions.

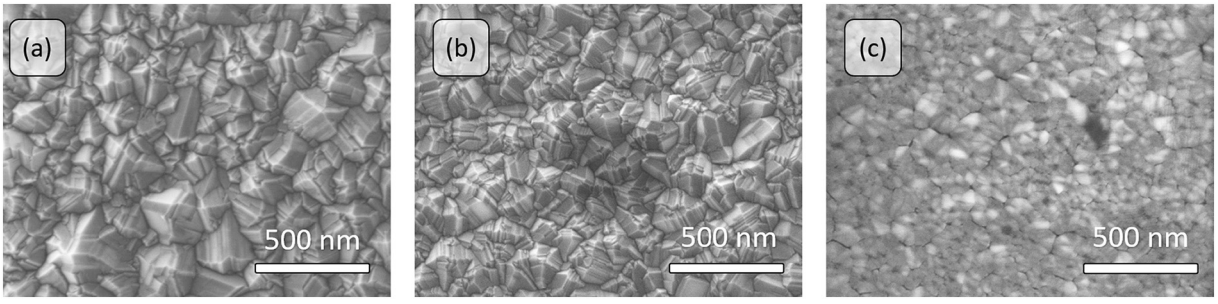

Fig. 2. The growth surface morphology of diamond sheets produced with different boron concentrations in the gas phase: (a) [B]/[C] = 250 ppm, (b) [B]/[C] = 20,000 ppm. (c) Nucleation surface morphology of the diamond sheet grown with [B]/[C] = 20,000 ppm.

nucleation surface is very smooth (Fig. 2c) and the grain boundaries (darker narrow trenches) and the bottom side of the grains (light gray regions) are well visible. The low surface roughness of approx. 12 nm was measured on the bottom nucleation surface using Atomic Force Microscopy, while average roughness of 67 nm was recorded on the top surface ([B]/[C] = 10,000 ppm) [40]. Few nano-sized gaps in the nucleation surface can be observed as well. These are likely caused by the detachment of individual grains. The average grain radius at the nucleation side is approx. 50 nm and an averaged grain (nucleation) density of 2×10^{11} cm^{-2} is calculated [40]. The mean planar grain radius (extracted from the growth surface) as a function of the boron level in the gas phase is presented in Fig. 3. The strong reduction in grain size, even for relatively low boron levels (250–1000 ppm), is evident.

Fig. 4 shows the Raman spectra of the BDD sheets as a function of the [B]/[C] ratio in the gas phase. At a relatively low [B/C] ratio, the diamond zone center phonon line located at around 1332 cm^{-1} [47] is the most pronounced signal. Increasing boron level up to 20,000 ppm leads to the appearance of the asymmetric bands centered around 500 cm^{-1} and 1200 cm^{-1}. These two features appear to be strongly connected to the boron concentration and, although their origin has been considered controversial [37,48], they have been linked to the disorder, intra-band optical transitions and B—C vibrations, among others.

Moreover, the Raman spectra of the diamond sheets consist of two characteristic bands around 1350 cm^{-1} and 1550 cm^{-1}, which are attributed to the sp^2 phase [47,49]. The Fano effect, i.e. 'deformation' and notable red-shift of the diamond line, is only observed for the

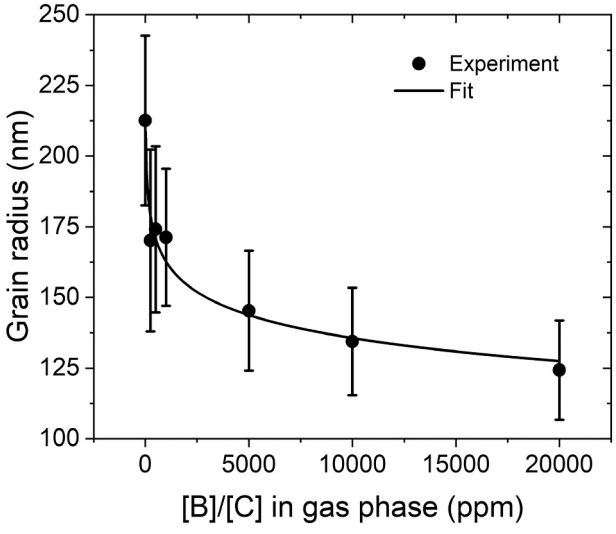

Fig. 3. The average planar grain radius of the diamond sheets as a function of [B/C] ratio (in ppm) in the gas phase. Experimental data (circles) are shown with logarithmic fitting curve. The error bars represent the standard error of the mean.

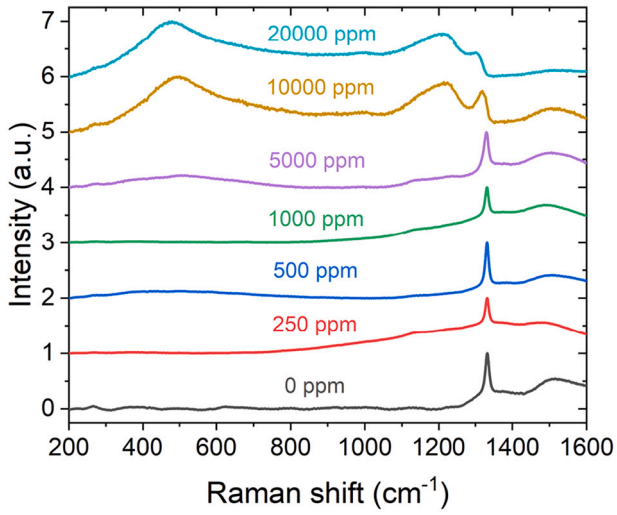

Fig. 4. Raman spectra of the diamond sheets as a function of [B]/[C] ratio in the gas phase.

samples prepared with a [B/C] ratio of 10,000 and 20,000 ppm. The shift of the sp^3-carbon Raman peak position is caused by the increase in B-doping level [50], different grain sizes and shapes [45], and boundary densities [51]. As a result, a variation in residual stresses is observed [52].

The '500 cm^{-1}' band for the diamond sheets prepared with a [B/C] ratio of 10,000 and 20,000 ppm can be fitted by a Lorentzian and a Gaussian component to determine the boron concentration in the films [48]. The results are shown in Fig. 5. Unfortunately, the equations proposed by Bernard et al. [48] and Mortet et al. [37] do not allow the estimation of the boron concentration in the low-doped BDD samples. Furthermore, the sample grown with [B]/[C] = 10,000 ppm is at the limit of applicability of the respective formulas. For this reason, the SIMS and Hall-effect measurements were used to determine the boron concentration within the two specific samples produced with a gas-phase [B/C] ratio of 250 and 10,000 ppm, respectively. The lowest doped sample is characterized by the boron concentration of 4.5×10^{17} atoms/cm^3, while the boron concentration for the highest doped

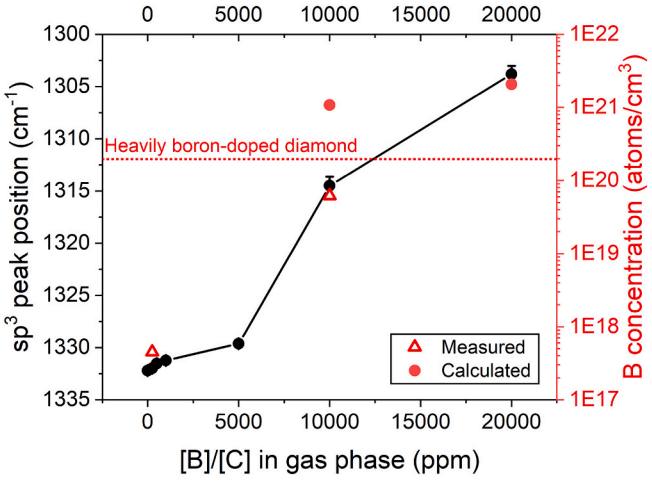

Fig. 5. The variation of the sp^3-carbon Raman peak (black) and the boron concentration in the BDD sheets (red) as a function of the boron level in the gas phase. The calculated B-concentration data in the samples were derived from Raman spectral data whereas the measured data were derived from SIMS and Hall-effect measurements. The error bars represent the standard error of the mean. The standard error of the mean boron concentration did not exceed 4 % of the mean value.

diamond sheet is four orders of magnitude higher. The differences in boron concentration (BDD with [B]/[C] = 10,000 ppm) obtained by Raman spectroscopy and Hall effect measurements, respectively, are because Hall measurements estimate only the distribution of the activated implanted atoms [53].

The determination of the optical band gap (E_g) was done via the Tauc plot; $(\alpha h\nu)^{1/2}$ was plotted against the phonon energy ($h\nu$). Here, α represents the optical absorption coefficient calculated from absorption spectra of the diamond sheets. The obtained results were determined from the intercept of the straight-line portion of the Tauc plots at $\alpha = 0$. The variation of the calculated optical band gap of the diamond sheets on PDMS and absorbance are presented in Table 1. The optical band gap decreases with increasing [B/C] ratio, i.e. boron doping level. For undoped diamond sheets it is 2.34 eV, while for [B]/[C] = 10,000 ppm it is 1.50 eV. The reduction of the optical band gap is accompanied by a reduction of ordered sp^3 carbon (diamond phase) [54]. Our results confirm that the optical band gap strongly depends on boron doping level showing values comparable with previous results on BDD thin films deposited on fused silica [36] and low-roughness thin C/diamond membranes obtained by Silva et al. [55]. The low optical band gap for the undoped sheets could be also affected by the termination of H atoms [56]. H-terminated surface will induce a p-type surface channel under atmospheric conditions [57]. Moreover, the optical properties of nanocrystalline diamond are strongly correlated with the size of sp^2 clusters [58,59]. Their increase causes a decrease in the optical band gap [60]. Ultimately, this experiment demonstrates the possibility of band gap widening/narrowing of diamond nano/micro-sheets by boron doping [61–64].

Fig. 6 (a) shows the systematic variation of the conductance versus temperature for boron levels ranging from [B]/[C] = 250 ppm to [B]/[C] = 20,000 ppm. The highest doped sample ([B/C] = 20,000 ppm) exhibits the highest conductance, being virtually constant across the entire temperature range (153–473 K) studied. Reduced boron concentration in our samples leads to a dramatic decrease in conductance, particularly visible at lower temperatures (<250 K). A similar trend is also observed at higher temperatures (393–473 K), although the variations between the samples are less pronounced, except for the sample prepared with [B]/[C] = 250 ppm, which shows an overall much lower conductance.

In further analysis, a model applied by Mott and Twose [66] and Fritzsche [67] was used. The electrical conductivity of the diamond sheets can be expressed by the below equation:

$$\sigma = A_1 exp(-E_1/kT) + A_2 exp(-E_2/kT) + A_3 exp(-E_3/kT) \quad (1)$$

where k is the Boltzmann constant, A_1, A_2, A_3 are doping and compensation-dependent constants, T is the absolute temperature and E_1, E_2, E_3 represent activation energies associated with three different conduction mechanisms. Empirically, activation energies follow the relation $E_1 > E_2 > E_3$, where E_1 is the energy required to lift an electron

Table 1
The optical band gap and absorbance of the B-doped nanocrystalline diamond sheets transferred to PDMS versus [B]/[C] ratio in the gas phase.

[B]/[C] ratio in the gas phase (ppm)	Optical band gap (eV)	Absorbance (a.u.)		
		400 nm	700 nm	1000 nm
0	2.34	0.26	0.17	0.14
250	2.32	0.32	0.18	0.16
500	2.30	0.38	0.22	0.19
1000	2.09	0.33	0.22	0.20
5000	1.97	0.33	0.35	0.44
10,000	1.50	0.44	0.63	1.03
20,000	*	0.75	0.94	0.88

* The sample exhibits metallic conductivity (see Fig. 6 (a)). The impurity band of the BDD sheet seems to be merged with the conduction band [65].

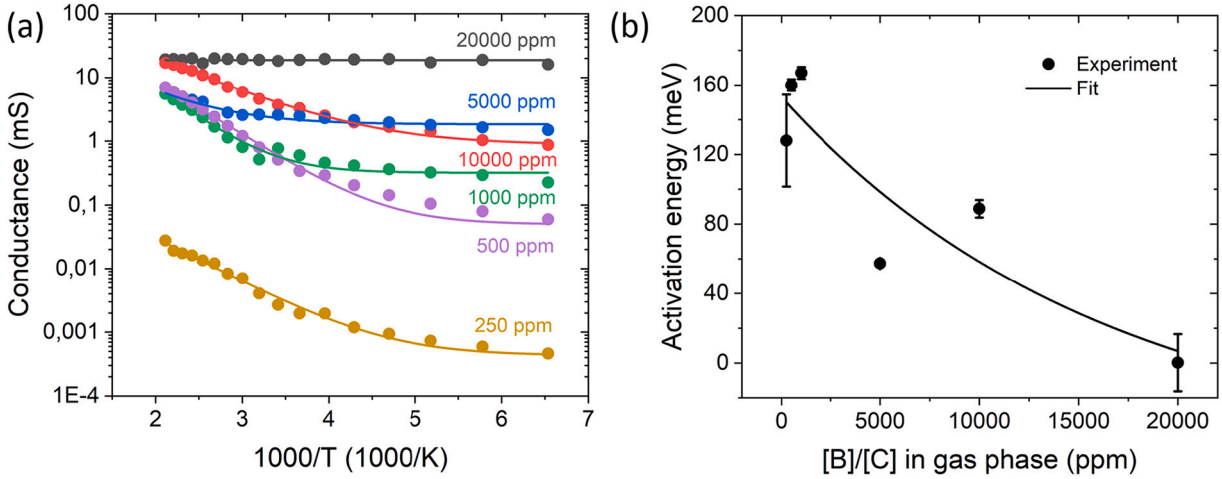

Fig. 6. Electrical measurements as a function of temperature and [B]/[C] ratio in the gas phase: (a) conductance of the diamond sheets versus 1000/T, (b) extracted activation energies calculated for the high-temperature range (> 393 K) with exponential fitting curve. The standard error of the mean conductance did not exceed 2.5 % of the mean value for a single measurement.

from the valence to the conduction band, around 5.47 eV in diamond [68]. E_2 can be neglected [67,69] as it occurs in a narrow doping range, and E_3 is the energy required for thermally activated nearest-neighbor hopping between boron dopants in the impurity band which lies 370 meV above the valence band [33]. The contribution from the first term in eq. 1 to the total conductivity is negligibly small compared to the third term, because E_1 is much larger than E_3. Thermal activation from the valence band into the impurity band thus dominates charge transport. The valence-band conduction can be written as follows:

$$\sigma_{vb} = q\mu p \tag{2}$$

where q is the elementary charge, μ is the mobility, and p the hole concentration. Constant A_3 in eq. 1 can be expressed as:

$$A_3 = A_{31} exp\left(-\left(A_{32} N_A^{-1/3}\right)\right) \tag{3}$$

where $A_{31} = 283.3\ \Omega^{-1}\ cm^{-1}$, $A_{32} = 2.16 \times 10^7\ cm^{-1}$, and N_A is the acceptor concentration [69].

Each measurement (except for [B]/[C] = 20,000 ppm in the gas phase) in Fig. 6 (a) is fit to $\sigma = A_3 exp(-E_3/kT)$ using the method of least squares, where A_3 is defined in eq. 3. N_A and E_3 are fitting parameters. E_3 represents the activation energy for thermal hopping across an energy barrier. Extracted activation energy E_3 versus boron dopant concentration in the high-temperature regime (393–473 K) is plotted in Fig. 6 (b). The activation energy decreases with increasing boron concentration as the impurity band is formed. At the lowest doping level (i.e., [B/C] = 250 ppm in the gas phase), the activation energy derived is 150 meV, more than a factor of two off from the theoretically expected activation energy of 370 meV for a single crystal diamond [70]. Lower doping levels are assumed to approach this literature value. We conclude that transport at room temperature is due to thermally activated nearest-neighbor hopping between boron dopants through impurity band conduction. At low temperatures (<300 K), the Arrhenius plot shows a non-linear temperature dependence of the logarithmic conductance pointing towards a crossover towards variable range hopping [71], following results obtained in previous studies [26,72].

To investigate the interactions between diamond sheets and graphene, we fabricated two types of heterojunctions (D-on-G) presented in Fig. 1. The diamond sheets with [B]/[C] = 500 ppm and 20,000 ppm were used, respectively. Fig. 7 shows the current-voltage characteristics of realized devices.

The key factors influencing the behavior of graphene-diamond vertical junctions includes boron doping and surface termination. Grown diamond sheets are predominantly hydrogen-terminated revealing a

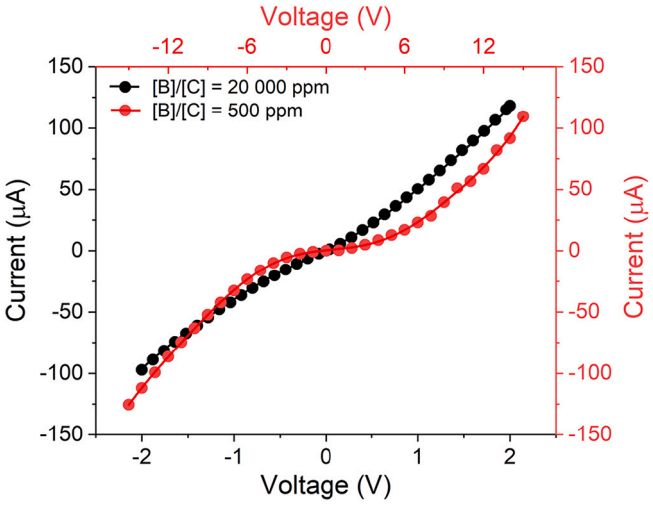

Fig. 7. I-V characteristics of fabricated graphene-diamond vertical junctions. Experimental data (circles) are shown with polynomial fitting curves. Note the different voltage scales on the respective x-axes.

highly conductive surface channel [73], while the electrons are transported from the conduction band irrespective of the surface termination [74]. Wan et al. [75] showed that the graphene causes a strong band bending on hydrogen-terminated diamond surface, lowering the binding energy of the valence band by approx. 150 meV. A descending surface band bending is also achieved by boron doping and hydrogen surface termination. As a consequence, the Fermi level of BDD films lies above values reported for graphene [76]. Thus, the electron transfer is observed across the junction reducing the diamond downward band bending. Furthermore, the lattice defects induced by the dopants favor a more pronounced charge transfer between graphene and diamond [77], and increase of the boron concentration weakens the bonds between the carbon bilayers, resulting in the formation of sp^2 bonds [78]. As a result, the current-voltage characteristic involving the diamond sheet prepared with [B]/[C] = 20,000 ppm is more linear than that recorded with the sample [B]/[C] = 500 ppm. The value of the Pearson's correlation coefficient is 0.99 for the device with [B]/[C] = 20,000 ppm, while for [B]/[C] = 500 ppm it is equal to 0.97. The vertical heterojunction with the lower boron concentration resembles a Schottky junction [79], while an almost Ohmic contact response is recorded with the BDD sheet of

metallic conductivity along with hydrogen termination.

Moreover, the transport of charges is facilitated for the device with higher doping. The obtained current (at 2 V applied voltage) for the device with [B]/[C] = 20,000 ppm is 118 μA, while it is only 2.2 μA for the one realized with [B]/[C] = 500 ppm.

Presented data confirms that thin-film diamond sheets with different boron concentrations allow for tailoring shapes of I-V curves in electronic junctions. Such an approach could be applied in the fabrication of elastic high-power devices utilizing ultra-thin flexible silicon or fused silica substrates since diamond could be elastically stretched even up to 10 % [30,40].

4. Conclusions

In this work, we have investigated the electrical, morphological, and optical properties of nanocrystalline diamond sheets as a function of boron doping. BDD thin sheets were fabricated in a microwave plasma-enhanced chemical vapor deposition reactor by varying the [B]/[C] ratio in the gas phase. The morphological studies revealed that the average surface grain size is nonlinearly dependent on the boron level. Additionally, an increase of disordered carbon content is accompanied by a lowering of the optical band gap with increasing boron levels.

The electrical properties of the diamond sheets are controlled by the concentration of boron. Metallic type of conductivity is observed for [B]/[C] = 20,000 ppm, while the rest of the samples present p-type conductivity. Charge transport at room temperature is due to thermally activated nearest-neighbor hopping between boron dopants through impurity band conduction. At low temperatures (<300 K), the Arrhenius plot shows a nonlinear temperature dependence of the logarithmic conductance pointing to a crossover towards variable range hopping.

Finally, as a proof of concept, we presented the I-V characteristics of vertical heterojunctions of graphene and low/highly doped BDD sheets. The current-voltage characteristic of the device structure realized with diamond using [B]/[C] = 20,000 ppm is more linear than that obtained with [B]/[C] = 500 ppm. Moreover, the transport of charges is greatly facilitated for a device with higher boron doping. This experiment could serve as a stepping stone in the future production of flexible high-power devices.

CRediT authorship contribution statement

Michał Rycewicz: Conceptualization, Investigation, Formal analysis, Visualization, Writing - Original Draft, Project administration. ***Adrian Nosek:*** Conceptualization, Formal analysis, Writing - Original Draft. ***Dong Hoon Shin:*** Conceptualization, Investigation, Writing - Review. ***Mateusz Ficek:*** Investigation, Project administration. ***Josephus G. Buijnsters:*** Supervision, Resources, Formal analysis, Writing - Review & Editing, Funding acquisition, Project administration. ***Robert Bogdanowicz:*** Supervision, Resources, Formal analysis, Writing - Review & Editing, Funding acquisition.

Declaration of competing interest

The authors declare that they have no known competing financial interests or personal relationships that could have appeared to influence the work reported in this paper.

Acknowledgments

M.R. acknowledges the financial support of the National Agency for Academic Exchange under the Iwanowska Programme (PPN/IWA/2019/1/00091/U/00001). D.H.S acknowledges funding by the KIND postdoctoral fellow program of the Kavli Institute of Nanoscience Delft. J.G.B acknowledges the Dutch Research Council (NWO) for funding through the Open Technology Programme (project no. 16361). The financial support from the Gdańsk University of Technology under the Plutonium grant (DEC-2/2020/IDUB/III.4.3/PU) is also acknowledged.

References

[1] J. Isberg, J. Hammersberg, E. Johansson, T. Wikström, D.J. Twitchen, A. J. Whitehead, S.E. Coe, G.A. Scarsbrook, High carrier mobility in single-crystal plasma-deposited diamond, Science 297 (2002) 1670–1672.
[2] T. Cheng, Z. Liu, Z. Liu, High elastic moduli, controllable bandgap and extraordinary carrier mobility in single-layer diamond, J. Mater. Chem. C 8 (2020) 13819–13826.
[3] C.J.H. Wort, R.S. Balmer, Diamond as an electronic material, Mater. Today 11 (2008) 22–28.
[4] P. Reinke, F. Benkhelifa, L. Kirste, H. Czap, L. Pinti, V. Zürbig, V. Cimalla, C. Nebel, O. Ambacher, Influence of different surface morphologies on the performance of high-voltage, low-resistance diamond Schottky diodes, IEEE Trans. Electron Devices 67 (2020) 2471–2477.
[5] J.E. Graebner, Thermal conductivity of diamond diamond: electronic properties and applications, in: L.S. Pan, D.R. Kania (Eds.), The Kluwer International Series in Engineering and Computer Science, Springer US, Boston, MA, 1995, pp. 285–318.
[6] V.I. Kleshch, S.T. Purcell, A.N. Obraztsov, Single crystal diamond needle as point electron source, Sci. Rep. 6 (2016) 35260.
[7] R. Kalish, Doping of diamond, Carbon 37 (1999) 781–785.
[8] S. Kunuku, M. Ficek, A. Wieloszynska, M.D. Tamulewicz-Szwajkowska, K. Gajewski, M. Sawczak, A. Lewkowicz, J. Ryl, T. Gotszalk, R. Bogdanowicz, Influence of B/N co-doping on electrical and photoluminescence properties of CVD grown homoepitaxial diamond films, Nanotechnology 33 (2021) 125603.
[9] E. Gheeraert, N. Casanova, A. Tajani, A. Deneuville, E. Bustarret, J.A. Garrido, C. E. Nebel, M. Stutzmann, n-Type doping of diamond by sulfur and phosphorus, Diamond and Related Materials 11 (2002) 289–295.
[10] C.E. Bradley, J. Randall, M.H. Abobeih, R.C. Berrevoets, M.J. Degen, M.A. Bakker, M. Markham, D.J. Twitchen, T.H. Taminiau, A ten-qubit solid-state spin register with quantum memory up to one minute, Phys. Rev. X 9 (2019) 031045.
[11] S.M. Nkambule, J.E. Lowther, Crystalline and random "diamond-like" boron–carbon structures, Solid State Communications 150 (2010) 133–136.
[12] E.A. Ekimov, V.A. Sidorov, E.D. Bauer, N.N. Mel'nik, N.J. Curro, J.D. Thompson, S. M. Stishov, Superconductivity in diamond, Nature 428 (2004) 542–545.
[13] V.A. Sidorov, E.A. Ekimov, E.D. Bauer, N.N. Mel'nik, N.J. Curro, V. Fritsch, J. D. Thompson, S.M. Stishov, A.E. Alexenko, B.V. Spitsyn, Superconductivity in boron-doped diamond, Diam. Related Materials 14 (2005) 335–339.
[14] S. Mandal, C. Naud, O.A. Williams, É. Bustarret, F. Omnès, P. Rodière, T. Meunier, L. Saminadayar, C. Bäuerle, Nanostructures made from superconducting boron-doped diamond, Nanotechnology 21 (2010) 195303.
[15] V. Jha, H. Surdi, M. Faizan Ahmad, F. Koeck, R.J. Nemanich, S. Goodnick, T. J. Thornton, Diamond schottky p-i-n diodes for high power RF receiver protectors, Solid State Electron. 186 (2021), 108154.
[16] H. Umezawa, M. Nagase, Y. Kato, S. Shikata, High temperature application of diamond power device, Diam. Relat. Mater. 24 (2012) 201–205.
[17] J.A. Cuenca, T. Brien, S. Mandal, S. Manifold, S. Doyle, A. Porch, G.M. Klemencic, O.A. Williams, Superconducting Boron Doped Nanocrystalline Diamond Microwave Coplanar Resonator, 2022.
[18] G.M. Klemencic, D.T.S. Perkins, J.M. Fellows, C.M. Muirhead, R.A. Smith, S. Mandal, S. Manifold, M. Salman, S.R. Giblin, O.A. Williams, Phase slips and metastability in granular boron-doped nanocrystalline diamond microbridges, Carbon 175 (2021) 43–49.
[19] N.A. Ahmad, R.A. Rahim, N.S. Ismail, B. Rezek, Fabrication of electrolyte-gate nanocrystalline diamond- based field effect transistor (NCD-EGFET) for HIV-1 Tat protein detection, IOP Conf. Ser.: Mater. Sci. Eng. 743 (2020) 012038.
[20] K.-S. Song, G.-J. Zhang, Y. Nakamura, K. Furukawa, T. Hiraki, J.-H. Yang, T. Funatsu, I. Ohdomari, H. Kawarada, Label-free DNA sensors using ultrasensitive diamond field-effect transistors in solution, Phys. Rev. E 74 (2006) 041919.
[21] Y. Sasama, T. Kageura, K. Komatsu, S. Moriyama, J. Inoue, M. Imura, K. Watanabe, T. Taniguchi, T. Uchihashi, Y. Takahide, Charge-carrier mobility in hydrogen-terminated diamond field-effect transistors, J. Appl. Phys. 127 (2020), 185707.
[22] Y. Sasama, K. Komatsu, S. Moriyama, M. Imura, T. Teraji, K. Watanabe, T. Taniguchi, T. Uchihashi, Y. Takahide, High-mobility diamond field effect transistor with a monocrystalline h-BN gate dielectric, APL Materials 6 (2018) 111105.
[23] Y. Kim, D. Lee, S.Y. Kim, E. Kang, C.K. Kim, Nanocomposite synthesis of nanodiamond and molybdenum disulfide, Nanomaterials 9 (2019) 927.
[24] F. Zhao, A. Vrajitoarea, Q. Jiang, X. Han, A. Chaudhary, J.O. Welch, R.B. Jackman, Graphene-Nanodiamond Heterostructures and their application to High Current Devices Sci Rep 5 (2015) 13771.
[25] Y. Wang, M. Jaiswal, M. Lin, S. Saha, B. Özyilmaz, K.P. Loh, Electronic properties of nanodiamond decorated graphene, ACS Nano 6 (2012) 1018–1025.
[26] R. Bogdanowicz, M. Ficek, M. Sobaszek, A. Nosek, Ł. Gołuński, J. Karczewski, A. Jaramillo-Botero, W.A. Goddard III, M. Bockrath, T. Ossowski, Growth and isolation of large area boron-doped nanocrystalline diamond sheets: a route toward diamond-on-graphene heterojunction, Adv. Funct. Mater. 29 (2019) 1805242.
[27] S.D. Janssens, S. Drijkoningen, K. Haenen, Ultra-thin nanocrystalline diamond membranes as pressure sensors for harsh environments, Appl. Phys. Lett. 104 (2014), 073107.
[28] R. Bogdanowicz, M. Ficek, N. Malinowska, S. Gupta, R. Meek, P. Niedziałkowski, M. Rycewicz, M. Sawczak, J. Ryl, T. Ossowski, Electrochemical performance of thin free-standing boron-doped diamond nanosheet electrodes, J. Electroanal. Chem. 862 (2020), 114016.

[29] K. Bray, H. Kato, R. Previdi, R. Sandstrom, K. Ganesan, M. Ogura, T. Makino, S. Yamasaki, A.P. Magyar, M. Toth, I. Aharonovich, Single crystal diamond membranes for nanoelectronics, Nanoscale 10 (2018) 4028–4035.
[30] C. Dang, J.-P. Chou, B. Dai, C.-T. Chou, Y. Yang, R. Fan, W. Lin, F. Meng, A. Hu, J. Zhu, J. Han, A.M. Minor, J. Li, Y. Lu, Achieving large uniform tensile elasticity in microfabricated diamond, Science 371 (2021) 76–78.
[31] J. Achard, F. Silva, R. Issaoui, O. Brinza, A. Tallaire, H. Schneider, K. Isoird, H. Ding, S. Koné, M.A. Pinault, F. Jomard, A. Gicquel, Thick boron doped diamond single crystals for high power electronics, Diam. Relat. Mater. 20 (2011) 145–152.
[32] D.J. Poferl, N.C. Gardner, J.C. Angus, Growth of boron-doped diamond seed crystals by vapor deposition, J. Appl. Phys. 44 (1973) 1428–1434.
[33] P. Ashcheulov, J. Šebera, A. Kovalenko, V. Petrák, F. Fendrych, M. Nesládek, A. Taylor, Z. Vlčková Živcová, O. Frank, L. Kavan, M. Dračínský, P. Hubík, J. Vacík, I. Kraus, I. Kratochvílová, Conductivity of boron-doped polycrystalline diamond films: influence of specific boron defects, Eur. Phys. J. B 86 (2013) 1–9.
[34] A. Zieliński, R. Bogdanowicz, J. Ryl, L. Burczyk, K. Darowicki, Local impedance imaging of boron-doped polycrystalline diamond thin films, Appl. Phys. Lett. 105 (2014), 131908.
[35] S.D. Janssens, P. Pobedinskas, J. Vacik, V. Petráková, B. Ruttens, J. D'Haen, M. Nesládek, K. Haenen, P. Wagner, Separation of intra- and intergranular magnetotransport properties in nanocrystalline diamond films on the metallic side of the metal–insulator transition, New J. Phys. 13 (2011), 083008.
[36] M. Ficek, M. Sobaszek, M. Gnyba, J. Ryl, Ł. Gołuński, M. Smietana, J. Jasiński, P. Caban, R. Bogdanowicz, Optical and electrical properties of boron doped diamond thin conductive films deposited on fused silica glass substrates, Appl. Surf. Sci. 387 (2016) 846–856.
[37] V. Mortet, Z. Vlčková Živcová, A. Taylor, O. Frank, P. Hubík, D. Trémouilles, F. Jomard, J. Barjon, L. Kavan, Insight into boron-doped diamond raman spectra characteristic features, Carbon 115 (2017) 279–284.
[38] A.F. Azevedo, R.C. Mendes de Barros, S.H.P. Serrano, N.G. Ferreira, SEM and Raman analysis of boron-doped diamond coating on spherical textured substrates, Surf. Coat. Technol. 200 (2006) 5973–5977.
[39] ASTM E112-96, Standard Test Methods for Determining Average Grain Size (West Conshohocken), 2013.
[40] M. Rycewicz, M. Ficek, K. Gajewski, S. Kunuku, J. Karczewski, T. Gotszalk, I. Wlasny, A. Wysmołek, R. Bogdanowicz, Low-strain sensor based on the flexible boron-doped diamond-polymer structures, Carbon 173 (2021) 832–841.
[41] J. Tauc, Optical properties and electronic structure of amorphous ge and si, Mater. Res. Bull. 3 (1968) 37–46.
[42] J. Cifre, J. Puigdollers, M.C. Polo, J. Esteve, Trimethylboron doping of CVD diamond thin films, Diam. Relat. Mater. 3 (1994) 628–631.
[43] H. Zeng, A.R. Konicek, N. Moldovan, F. Mangolini, T. Jacobs, I. Wylie, P. U. Arumugam, S. Siddiqui, R.W. Carpick, J.A. Carlisle, Boron-doped ultrananocrystalline diamond synthesized with an H-rich/Ar-lean gas system, Carbon 84 (2015) 103–117.
[44] J.G. Buijnsters, L. Vázquez, Growth dynamics of nanocrystalline diamond thin films deposited by hot filament chemical vapor deposition: influence of low sticking and renucleation processes, J. Phys. Chem. C 115 (2011) 9681–9691.
[45] W. Gajewski, P. Achatz, O.A. Williams, K. Haenen, E. Bustarret, M. Stutzmann, J. A. Garrido, Electronic and optical properties of boron-doped nanocrystalline diamond films, Phys. Rev. B 79 (2009), 045206.
[46] J.G. Buijnsters, M. Tsigkourakos, T. Hantschel, F.O.V. Gomes, T. Nuytten, P. Favia, H. Bender, K. Arstila, J.-P. Celis, W. Vandervorst, Effect of boron doping on the wear behavior of the growth and nucleation surfaces of micro- and nanocrystalline diamond films, ACS Appl. Mater. Interfaces 8 (2016) 26381–26391.
[47] A. Merlen, J.G. Buijnsters, C. Pardanaud, A guide to and review of the use of multiwavelength raman spectroscopy for characterizing defective aromatic carbon solids: from graphene to amorphous carbons, Coatings 7 (2017) 153.
[48] M. Bernard, A. Deneuville, P. Muret, Non-destructive determination of the boron concentration of heavily doped metallic diamond thin films from raman spectroscopy, Diam. Relat. Mater. 13 (2004) 282–286.
[49] A.C. Ferrari, J.C. Meyer, V. Scardaci, C. Casiraghi, M. Lazzeri, F. Mauri, S. Piscanec, D. Jiang, K.S. Novoselov, S. Roth, A.K. Geim, Raman spectrum of graphene and graphene layers, Phys. Rev. Lett. 97 (2006), 187401.
[50] B. Dec, M. Ficek, M. Rycewicz, Ł. Macewicz, M. Gnyba, M. Sawczak, M. Sobaszek, R. Bogdanowicz, Gas composition influence on the properties of boron-doped diamond films deposited on the fused silica, Mater. Sci. Pol. 36 (2018) 288–296.
[51] J. Michler, Y. von Kaenel, J. Stiegler, E. Blank, Complementary application of electron microscopy and micro-raman spectroscopy for microstructure, stress, and bonding defect investigation of heteroepitaxial chemical vapor deposited diamond films, J. Appl. Phys. 83 (1998) 187–197.
[52] H. Li, T. Zhang, L. Li, X. Lü, B. Li, Z. Jin, G. Zou, Investigation on crystalline structure, boron distribution, and residual stresses in freestanding boron-doped CVD diamond films, Journal of Crystal Growth 312 (2010) 1986–1991.
[53] E. Zinner, Depth profiling by secondary ion mass spectrometry, Scanning 3 (1980) 57–78.
[54] S. Gupta, B.R. Weiner, G. Morell, Spectroscopic ellipsometry studies of nanocrystalline carbon thin films deposited by HFCVD, Diam. Relat. Mater. 10 (2001) 1968–1972.
[55] S.R.P. Silva, G.A.J. Amaratunga, C.P. Constantinou, D.R. McKenzie, Smooth thin film C/diamond membranes with controllable optical band gaps, Diam. Relat. Mater. 1 (1992) 612–618.
[56] S. Zhao, K. Larsson, Theoretical study of the energetic stability and geometry of terminated and B-doped diamond (111) surfaces, J. Phys. Chem. C 118 (2014) 1944–1957.
[57] H. Kawarada, Hydrogen-terminated diamond surfaces and interfaces, Surf. Sci. Rep. 26 (1996) 205–259.
[58] V. Ralchenko, S. Pimenov, V. Konov, A. Khomich, A. Saveliev, A. Popovich, I. Vlasov, E. Zavedeev, A. Bozhko, E. Loubnin, R. Khmelnitskii, Nitrogenated nanocrystalline diamond films: thermal and optical properties, Diam. Relat. Mater. 16 (2007) 2067–2073.
[59] C. Popov, W. Kulisch, M. Jelinek, A. Bock, J. Strnad, Nanocrystalline diamond/amorphous carbon composite films for applications in tribology, optics and biomedicine, Thin Solid Films 494 (2006) 92–97.
[60] A. Majumdar, S.C. Das, R. Bogdanowicz, T. Shripathi, W. Langel, R. Hippler, Role of nitrogen in evolution of sp2/sp3 bonding and optical band gap in hydrogenated carbon nitride, Vibrational Spectroscopy 66 (2013) 63–68.
[61] S. Choudhury, B. Kiendl, J. Ren, F. Gao, P. Knittel, C. Nebel, A. Venerosy, H. Girard, J.-C. Arnault, A. Krueger, K. Larsson, T. Petit, Combining nanostructuration with boron doping to alter sub band gap acceptor states in diamond materials, J. Mater. Chem. A 6 (2018) 16645–16654.
[62] L.T. Anh, F.C.I. Catalan, Y. Kim, Y. Einaga, Y. Tateyama, Boron position-dependent surface reconstruction and electronic states of boron-doped diamond(111) surfaces: an ab initio study, Phys. Chem. Chem. Phys. 23 (2021) 15628–15634.
[63] M. Ullah, E. Ahmed, F. Hussain, A.M. Rana, R. Raza, Electrical conductivity enhancement by boron-doping in diamond using first principle calculations, Appl. Surf. Sci. 334 (2015) 40–44.
[64] S. Ossicini, E. Degoli, F. Iori, E. Luppi, R. Magri, G. Cantele, F. Trani, D. Ninno, Simultaneously B- and P-doped silicon nanoclusters: formation energies and electronic properties, Appl. Phys. Lett. 87 (2005), 173120.
[65] T. Wakita, K. Terashima, T. Yokoya, in: Y. Kubozono (Ed.), Physics of Heavily Doped Diamond: Electronic States and Superconductivity Physics and Chemistry of Carbon-Based Materials: Basics and Applications, Springer, Singapore, 2019, pp. 65–96.
[66] N.F. Mott, W.D. Twose, The theory of impurity conduction, Advances in Physics 10 (1961) 107–163.
[67] H. Fritzsche, Electrical properties of germanium semiconductors at low temperatures, Phys. Rev. 99 (1955) 406–419.
[68] W. Saslow, T.K. Bergstresser, M.L. Cohen, Band structure and optical properties of diamond, Phys. Rev. Lett. 16 (1966) 354–356.
[69] M. Werner, R. Locher, Growth and application of undoped and doped diamond films rep, Prog. Phys. 61 (1998) 1665–1710.
[70] R.M. Chrenko, Boron, the dominant acceptor in semiconducting, Diam. Phys. Rev. B 7 (1973) 4560–4567.
[71] M. Pollak, A percolation treatment of DC hopping conduction, J. Non-Cryst. Solids 8–10 (1972) 486–491.
[72] B. Massarani, J.C. Bourgoin, R.M. Chrenko, Hopping conduction in semiconducting diamond, Phys. Rev. B 17 (1978) 1758–1769.
[73] T. Yamada, T. Masuzawa, H. Mimura, K. Okano, Field emission spectroscopy measurements of graphene/n-type diamond heterojunction, Appl. Phys. Lett. 114 (2019), 231601.
[74] T. Yamada, T. Masuzawa, H. Mimura, K. Okano, Electron emission from conduction band of heavily phosphorus doped diamond negative electron affinity surface, J. Phys. D. Appl. Phys. 49 (2015), 045102.
[75] G. Wan, S. Panditharatne, N.A. Fox, M. Cattelan, Graphene-diamond junction photoemission microscopy and electronic interactions, Nano Ex. 1 (2020), 020011.
[76] L. Diederich, O.M. Küttel, P. Aebi, L. Schlapbach, Electron affinity and work function of differently oriented and doped diamond surfaces determined by photoelectron spectroscopy, Surf. Sci. 418 (1998) 219–239.
[77] S. Zhao, K. Larsson, First principle study of the attachment of graphene onto non-doped and doped diamond (111), Diamond and Related Materials 66 (2016) 52–60.
[78] C. Lu, H. Yang, J. Xu, L. Xu, M. Chshiev, S. Zhang, C. Gu, Spontaneous formation of graphene on diamond (111) driven by B-doping induced surface reconstruction, Carbon 115 (2017) 388–393.
[79] A. Di Bartolomeo, Graphene schottky diodes: an experimental review of the rectifying graphene/semiconductor heterojunction, Phys. Rep. 606 (2016) 1–58.